



Development of an energy dissipation restrainer for bridges using a steel shear panel



Kailai Deng^a, Peng Pan^{c,*}, Yukun Su^a, Tianran Ran^a, Yantao Xue^b

^a Department of Civil Engineering, Tsinghua University, Beijing 100084, China

^b Institute of Building Structures, China Academy of Building Research, Beijing 100013, China

^c Key Laboratory of Civil Engineering Safety and Durability of the China Education Ministry, Department of Civil Engineering, Tsinghua University, Beijing 100084, China

ARTICLE INFO

Article history:

Received 1 October 2013

Accepted 31 March 2014

Available online 3 June 2014

Keywords:

Bridge

Restrainer

Energy dissipation capacity

Finite element model

Parameter fitting

ABSTRACT

Restrainers, along with isolation bearings, are often installed in bridges to avoid upper girders falling off their piers during large earthquakes. In this study, a novel energy dissipation restrainer was developed. The energy dissipation restrainer remains elastic and provides a reaction force to restrain the displacement of the girder during small earthquakes, maintaining the functionality of the bridges. When large earthquakes occur, the restrainer can yield and dissipate energy, thus reducing the deformation between the superstructures and piers, and protecting the piers from server damages. To verify the performance of the restrainer, five specimens were designed and subjected to physical loading tests. The test results suggest that when appropriately designed, the restrainer has satisfactory deformation and energy dissipation capacities. The thickness of the side flange and width of the energy dissipation plate have significant effects on its performance. Because the number of physical tests was limited, finite element models were built using the general finite element program ABAQUS to supplement the results, and a parametric study focusing on the effects of the side flange thickness and restrainer width was conducted. Based on the test and analysis results, a formula for estimating the restrainer strength was derived.

© 2014 Elsevier Ltd. All rights reserved.

1. Introduction

The unseating of superstructures is the most common failure mode for bridges when subjected to strong ground motion [1–3]. To prevent superstructures from dropping off piers, restrainers with adequate strength are usually installed in bridges to restrain the displacement of the superstructure [4]. Post-earthquake investigations suggest that bridges equipped with restrainers sustain only minor damage in earthquakes and there is no disruption to traffic [5,6].

Investigators have developed many types of restrainers, e.g., steel cables, concrete walls, steel plates, and shape memory alloy (SMA) devices. Numerical models of bridges with restrainers have been built and their response during earthquakes was analyzed [7,8]. The results obtained from the studies indicate that restrainers can effectively prevent the unseating of the superstructure and reduce the damage to the bridge.

There are mainly three types of restrainers, namely rigid, yielding, and SMA restrainers. The rigid restrainers, which are commonly made of concrete walls, are designed to completely restrain the displacement

of the superstructure of the bridge. Bridges with rigid restrainers have inadequate energy dissipation capacity; therefore, the acceleration of the superstructures and the shear of the piers in those bridges are greater than those of bridges with yielding and SMA restrainers during large earthquakes [9]. Moreover, rigid restrainers do not have good deformation capacity, leading to a brittle failure when large earthquakes occur, which requires difficult and lengthy repairs [5].

Much research on SMA restrainers has been carried out [10–13]. SMA restrainers can reduce the residual displacement of the superstructure and can dissipate large amounts of energy to reduce damage to the bridge. However, the properties of SMA materials are not necessarily stable when they sustain cyclic thermal or mechanical loading [14,15]. In addition, the costs of restrainers made of SMA are much higher than those made of most common metals.

Yielding restrainers, usually made of steel, have stable mechanical performance and are cost-effective. The response of bridges with yielding restrainers is very close to that of bridges with SMA restrainers [9]. Yielding restrainers made of reinforced concrete and steel have also been proposed [16,17]. These studies showed that properly designed yielding restrainers have good and stable mechanical properties and are suitable for engineering applications.

In this study, a novel energy dissipation restrainer for a bridge is proposed. The energy dissipation restrainer remains elastic and provides a

* Corresponding author. Tel.: +86 10 62794729; fax: +86 10 62788620.

E-mail address: panpeng@mail.tsinghua.edu.cn (P. Pan).

reaction force to restrain the displacement of the girder during small earthquakes, maintaining the functionality of the bridges. When large earthquakes occur, the restrainer can yield and dissipate energy, thus reducing the deformation between the superstructures and piers, and protecting the piers from server damages. To achieve the two-stage performance goals, the strength and deformation capacity of the restrainer are key parameters. In this paper the structure of the novel restrainer is presented first. Five specimens were designed and tested to investigate the mechanical properties of the restrainer. The test results indicate that an appropriately designed restrainer performs well mechanically. Because the number of specimens in our tests was limited, finite element (FE) analyses were carried out to supplement the physical tests. Finally, based on the tests and analysis results, a design formula for estimating the ultimate strength of the restrainer is proposed.

2. Structure of the restrainer

The restrainers are commonly installed with the isolation bearings between the upper girders and lower piers. As shown in Fig. 1, the restrainer consists of an energy dissipation plate and two horizontal locking blocks. The energy dissipation plate is fixed on the lower piers while the horizontal locking blocks are bolted to the bottom of the girder by high-strength bolts. Note that following the installation (Fig. 1, left) the restrainer only takes effect along the transverse direction of the bridge and does not provide resistance in both vertical and longitudinal directions. This is beneficial for easy installation and to guarantee the performance of the restrainer. The restrainer can also be used in the longitudinal direction by changing the installation angle (Fig. 1, right). When a superstructure is displaced relative to the piers, the horizontal locking blocks will force the energy dissipation plate to deform. During a small earthquake the energy dissipation plate remains elastic and provides reaction forces to restrain the displacement of the upper girder. When a large earthquake occurs it yields and dissipates the energy, thus reducing the responses of the bridge. The energy dissipation plate can be easily replaced if damaged, so the bridge can be quickly repaired after an earthquake. Small gaps, which is commonly about 2 mm, are set between the energy dissipation plate and the horizontal locking blocks for the convenience of installation and replacement. The horizontal locking blocks are designed to be rigid so that the deformation is concentrated in the energy dissipation plates; therefore, this study mainly focuses on the performance of these plates.

The details of the restrainer are shown in Fig. 2. The dimensions of the horizontal locking block are shown in the lower right corner of Fig. 2. A semi-circular piece of steel is welded onto the connection

plate to accurately determine the height of the contact point. To design the horizontal locking block we adopt a simple formula

$$f_y A > \lambda F_u \quad (1)$$

where f_y is the yield strength of the material and A is the area of the cross-section of the horizontal locking block. F_u is the total reaction force of the energy dissipation plate and λ is a conservative factor which should be larger than 1 to guarantee the horizontal locking block remaining elastic during an earthquake. We assume the maximum F_u to be 600 kN and f_y is set as 310 MPa. Setting $\lambda = 4$, A should be larger than 5655 mm². In Fig. 2, $A = 10,500$ mm², which meets the requirement of Eq. (1).

The web area of the dissipation plate is the main area for energy dissipation, outlined in bold in Fig. 2. The width and height of the web (w and h , respectively) are the main parameters relating to energy dissipation. The top flange and the side flange are welded to the web. A stiffener is added to prevent out-of-plane buckling of the web. Fillet welding, 6 mm thick, is used to weld the stiffener and flanges to the web. The energy dissipation restrainer works in a manner similar to that of shear panels, which are commonly used as steel dampers in building structures [18–20]. However, the vertical free mechanism and force concentration at the contacts between the energy dissipation plate and the horizontal locking blocks require the energy dissipation plate to have a different structure. To this end, we carried out physical tests to investigate its optimal design.

3. Testing procedure

The width of the energy dissipation plate w , the thickness of the top flange t , and the thickness of the side flange b were the main parameters in the tests. Five specimens were designed as shown in Table 1. S1 is the standard specimen in the study. The stiffeners of S1 were designed by following the requirements of a steel shear panel damper. S2 has thin side-flanges that are 6 mm thick. S3 has a thinner top flange which is 10 mm thick. In S4 the width of the web was reduced to 150 mm, and S5 has additional horizontal stiffeners. The web plates of all the specimens are 300 mm high and 6 mm thick. The stiffeners are 100 mm wide, and the side flanges are 200 mm wide.

The loading setup, consisting of an actuator and a loading frame, is shown in Fig. 3. The loading frame was fixed to the ground with anchor bolts. The horizontal locking blocks and the energy dissipation plate were connected to the upper loading frame and the lower base using high-strength bolts. The horizontal locking blocks, which are in contact

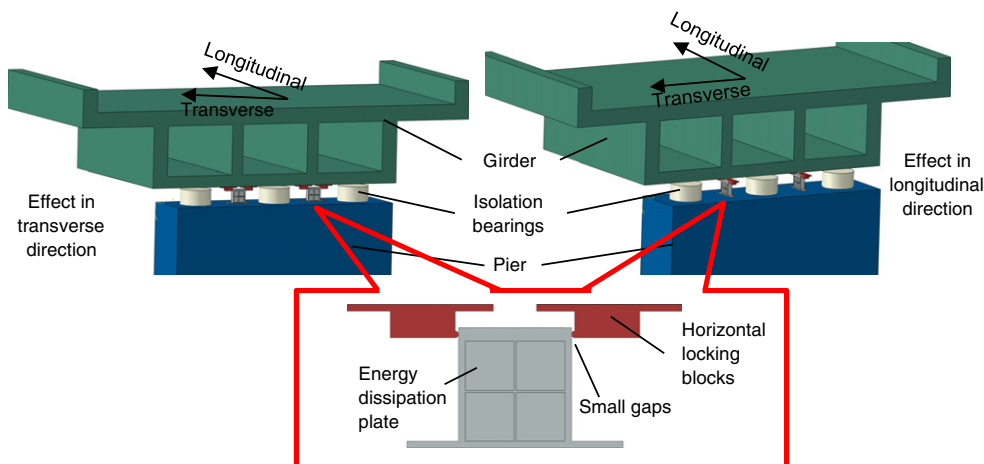


Fig. 1. Installation diagram of the restrainer.

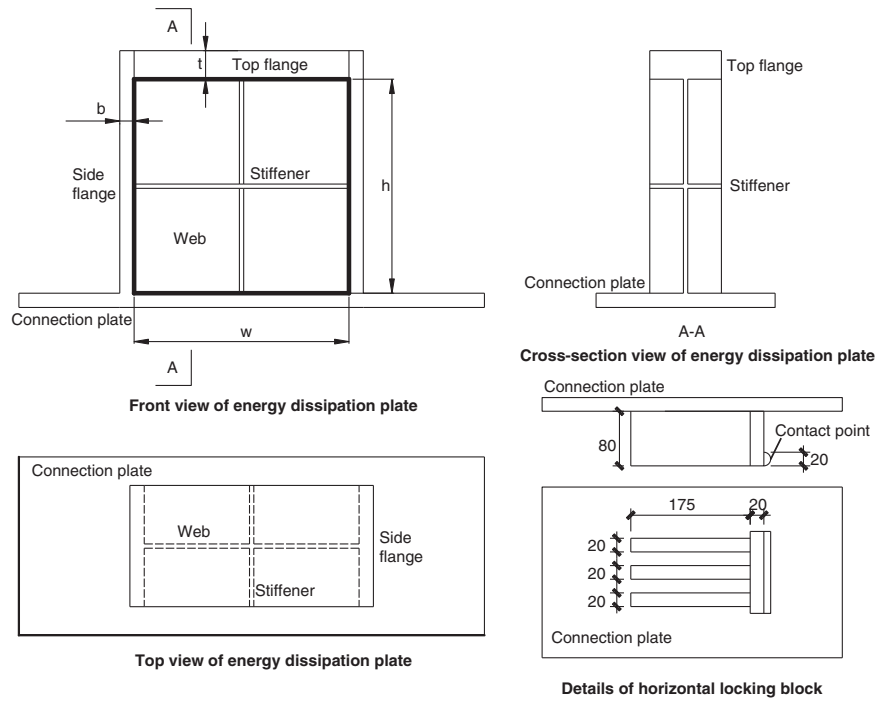


Fig. 2. Details of restrainer.

with the side flange of the energy dissipation plate, are 305 mm high. The loading frame has four pin connections at the beam to column connections, so that the frame can rotate freely. As the loading amplitude increases, the upper loading frame moves down slightly. In the test, the maximum loading amplitude was 54 mm, and the corresponding displacement of the upper loading frame was no more than 1 mm; therefore, the effect could be ignored. The forces exerted by the actuator are taken to be equal to the restoring forces provided by the restrainer.

The loading uses displacement control and the loading scheme is shown in Fig. 4. The restrainer is loaded to amplitudes of 3 and 6 mm for three cycles. The loading displacement amplitude increases in steps of 6–54 mm. For each loading amplitude the restrainer is loaded for three cycles.

Five displacement transducers, designated D1 to D5, are installed on the specimen (Fig. 5). D1 measures the relative displacement of the top flange to the base, which is expected to be the loading control displacement. D2 and D3 are installed on the left and right sides of the energy dissipation plate to record its bending deformation. The distance from D2 to D3 is l_2 and the bending deformation can be calculated using Eq. (2).

$$R_b = \frac{D_2 - D_3}{l_2} \quad (2)$$

where R_b represents the bending deformation angle of the energy dissipation plate. The shear deformation can be calculated using Eq. (3) [21].

$$R_s = \frac{\sqrt{h^2 + l_1^2}}{2hl_1} (D_4 - D_5) \quad (3)$$

where R_s represents the shear deformation angle and D_4 and D_5 measure the diagonal displacement to obtain the shear deformation of the energy dissipation plate. h is the height of the web, and l_1 is equal to the width of the web. Thus, the ratio of shear deformation to total deformation r_s can be calculated as

$$r_s = \frac{R_s}{R_s + R_b} \quad (4)$$

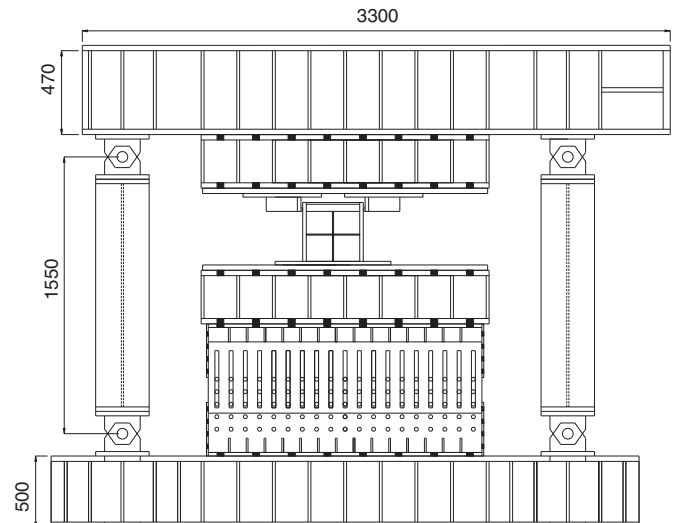


Fig. 3. Details of test setup.

Table 1
Parameters of five specimens.

No.	b (mm)	t (mm)	w (mm)	Stiffener (vertical * horizontal)
S1	20	40	300	1 * 1
S2	6	40	300	1 * 1
S3	20	10	300	1 * 1
S4	20	40	150	0 * 1
S5	20	40	300	1 * 2

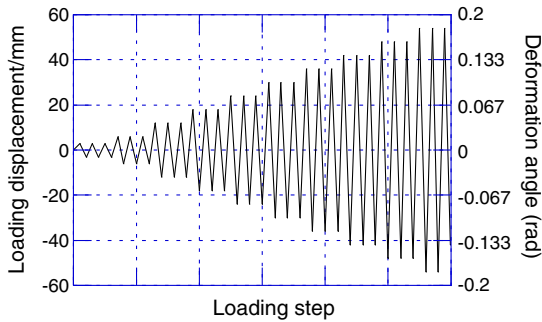


Fig. 4. Loading scheme.

4. Experimental results

4.1. Deformation and failure modes

The deformation modes of S1 to S5 are shown in Fig. 6a, c, e, g, and i. Based on the data measured by transducers D2–D5 the shear deformation angles and bending deformation angles of the energy dissipation plates are plotted in Fig. 6b, d, f, h, and j.

S1 is the standard specimen. Buckling occurred on the side flange of S1, as shown in Fig. 6a. Because of the vertical free mechanism, the side flanges of the energy dissipation plate sustain large compressive and tensile forces during an earthquake. To avoid buckling, the side flanges must have good stability. In our tests, the web and the bottom of the side flange cracked in the first cycle of loading at an amplitude of 42 mm. The reaction force decreased in the first cycle of loading at 48 mm because of the low-cycle fatigue damage to the web and side flange. Fig. 6b shows the shear and bending deformation angles of S1. The horizontal axis represents the loading steps. S1 is dominated by the shear deformation, which takes up to 90% of the total deformation. Because of the buckling to the left side flange, S1 had a tendency to bend to the left, as shown in Fig. 6b. Unlike the standard specimen S1, S2 has side flanges that are 6 mm thick. The thinner side flanges of S2 could not resist the large axial force and it buckled significantly, reducing the height of the energy dissipation plate. The deformation mode of S2 is shown in Fig. 6c. Because of the buckling of the side flanges, the reaction force of S2 decreased in the first cycle of loading at an amplitude of 30 mm. Fig. 6d shows that the shear deformation of S2 takes up about 76% of the total deformation.

Unlike the standard specimen S1, the top flanges of S3 are 10 mm thick. Under the large concentrated load from the horizontal locking

blocks, significant local buckling occurred on the top flanges of S3 (Fig. 3e). Because of the buckling of the top flange, the reaction force of S3 decreased sharply. In the second cycle of loading at an amplitude of 24 mm, S3 could not provide an adequate reaction force. In addition, because of the local buckling of the top flange, the displacement transducer D2 dropped in the second cycle of loading at 18 mm. Fig. 6f shows that the shear deformation of S3 takes up about 87% of the total deformation.

In specimen S4, the web was 150 mm rather than 300 mm wide. The deformation mode of S4 was similar to that of S1, as shown in Fig. 6g. The side flanges buckled after sustaining large deformation. S4 lost its force capacity because of the low-cycle fatigue damage at the web and at the bottom of the side flanges. The shear and bending deformations of S4 are shown in Fig. 6h. The shear deformation of S4 dominated 88% of the total deformation, which was similar to the proportion of shear deformation for S1.

Specimen S5 had two horizontal stiffeners to strengthen the stability of the side flanges and web. As shown in Fig. 6i, this effectively suppressed the buckling of the side flanges. The comparison between the shear and bending deformations is shown in Fig. 6j for S5. Because of the strengthened side flanges, the shear deformation dominated 93% of the total deformation. The failure mode of S5 is similar to that of S1. Low cycle fatigue damage appeared at the bottom of the side flanges and web, as shown in Fig. 6i. The reaction force of S5 decreased at the third cycle of loading at an amplitude of 48 mm, showing that S5 has the best deformation capacity of the five specimens.

According to the above observations for the deformation and failure modes, we conclude that the side flanges require adequate stiffness to maintain stability under huge axial forces. To avoid local buckling, the top flange should be made of a steel plate of adequate thickness. Shear deformation is still dominant even for an energy dissipation plate with an aspect ratio of 2. Horizontal stiffeners are beneficial in improving the stability of the side flanges and web, thus increasing the deformation capacity of the restrainer.

4.2. Hysteretic performance

The hysteresis curves of the five specimens are summarized in Fig. 7. In the figures, the horizontal axis shows the displacement measured by displacement transducer D1, while the vertical axis is the reaction force exerted by the actuator. The hysteresis curve of S1 (Fig. 7a) is stable and saturated. The observed yield strength and ultimate strength of S1 were 270 and 568 kN, respectively. The reaction force decreased at the first cycle of loading at an amplitude of 48 mm because the web and bottom of the side flange cracked as a result of low-cycle fatigue damage.

Fig. 7b shows the hysteresis curve of S2, which was stable and saturated when the loading amplitude was less than 24 mm. However, the reaction force of S2 decreased sharply because of the significant buckling of the side flanges. The yield strength and ultimate strength of S2 were 250 and 462 kN, respectively. S2 could not be loaded further after the first cycle of loading at an amplitude of 30 mm.

The hysteresis curve of S3 is shown in Fig. 7c. Because of the local buckling of the top flange, the maximum loading displacement for S3 was 24 mm. The yield strength and ultimate strength of S3 were 272 and 515 kN, respectively.

Fig. 7d shows the hysteresis curve of S4, which was stable and saturated. The yield strength and ultimate strength of S4 were 176 and 332 kN, respectively. The web of S4 was 150 mm wide, which was exactly half the width of S1, while the strength was more than half that of S1. The results indicate that the side flanges provide part of the reaction force.

The hysteresis curve of S5 was stable and saturated, as shown in Fig. 7e. The yield strength and ultimate strength of S5 were 287 and 629 kN, respectively. The ultimate strength of S4 was obviously larger than that of S1. The results indicate that the horizontal stiffeners improve the stability of side flanges and increase the ultimate strength of

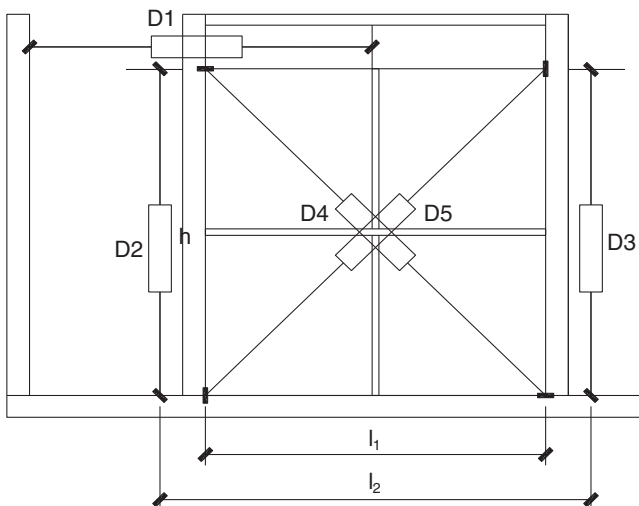
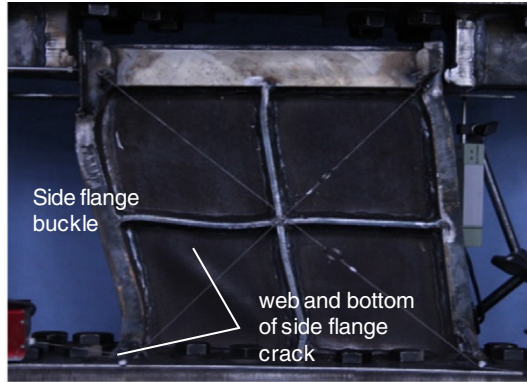
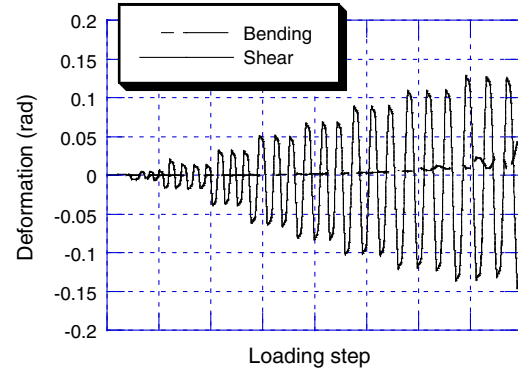


Fig. 5. Instrument of displacement transducers.

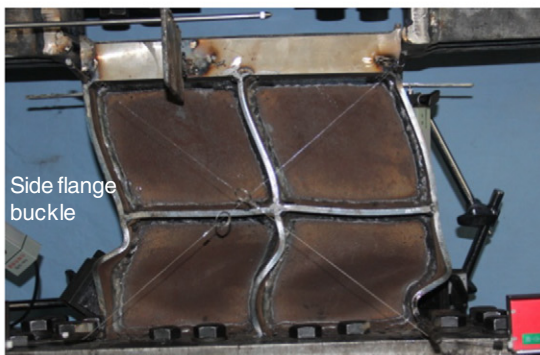
a) Deformation mode of S1



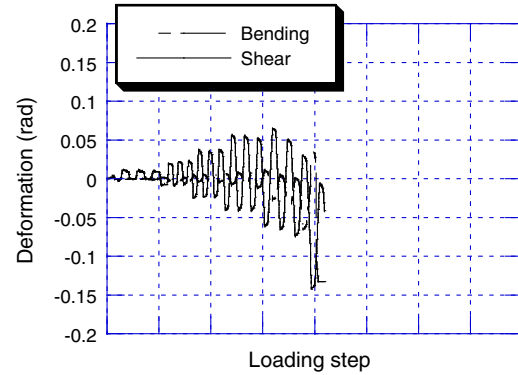
b) Shear and bending deformation ratio of S1



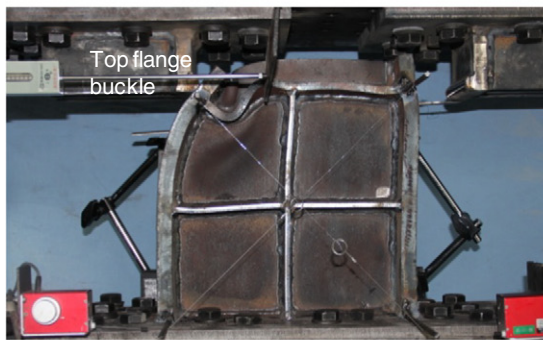
c) Deformation mode of S2



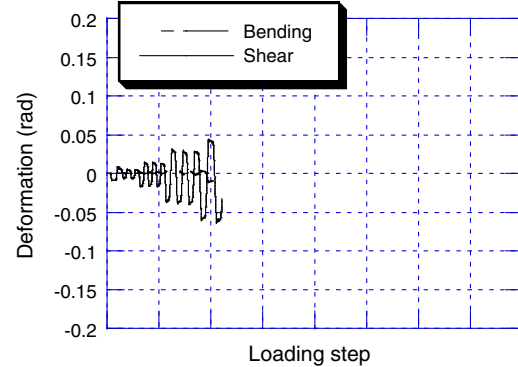
d) Shear and bending deformation ratio of S2



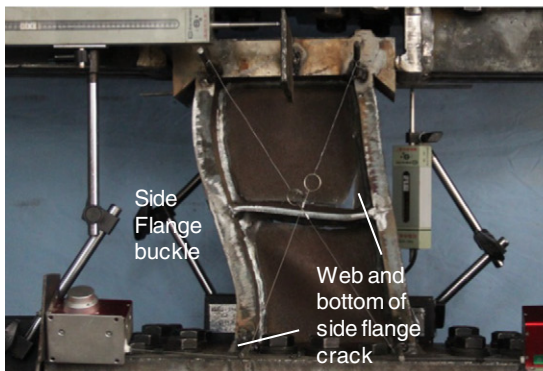
e) Deformation mode of S3



f) Shear and bending deformation ratio of S3



g) Deformation mode of S4



h) Shear and bending deformation ratio of S4

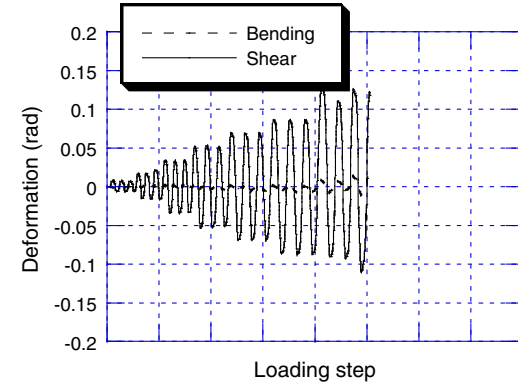
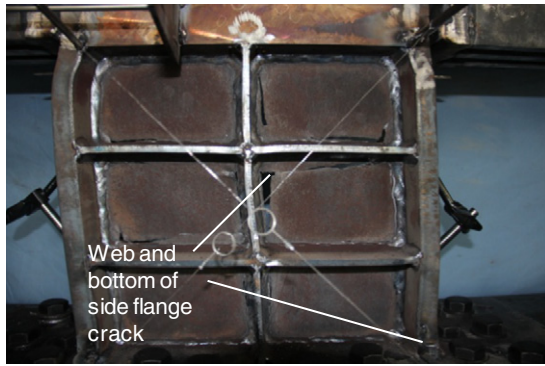


Fig. 6. Deformation mode.

i) Deformation mode of S5



j) Shear and bending deformation ratio of S5

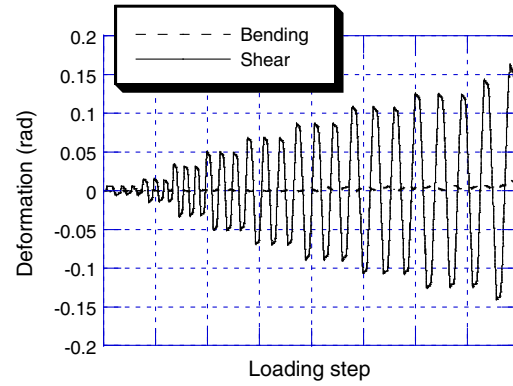


Fig. 6 (continued).

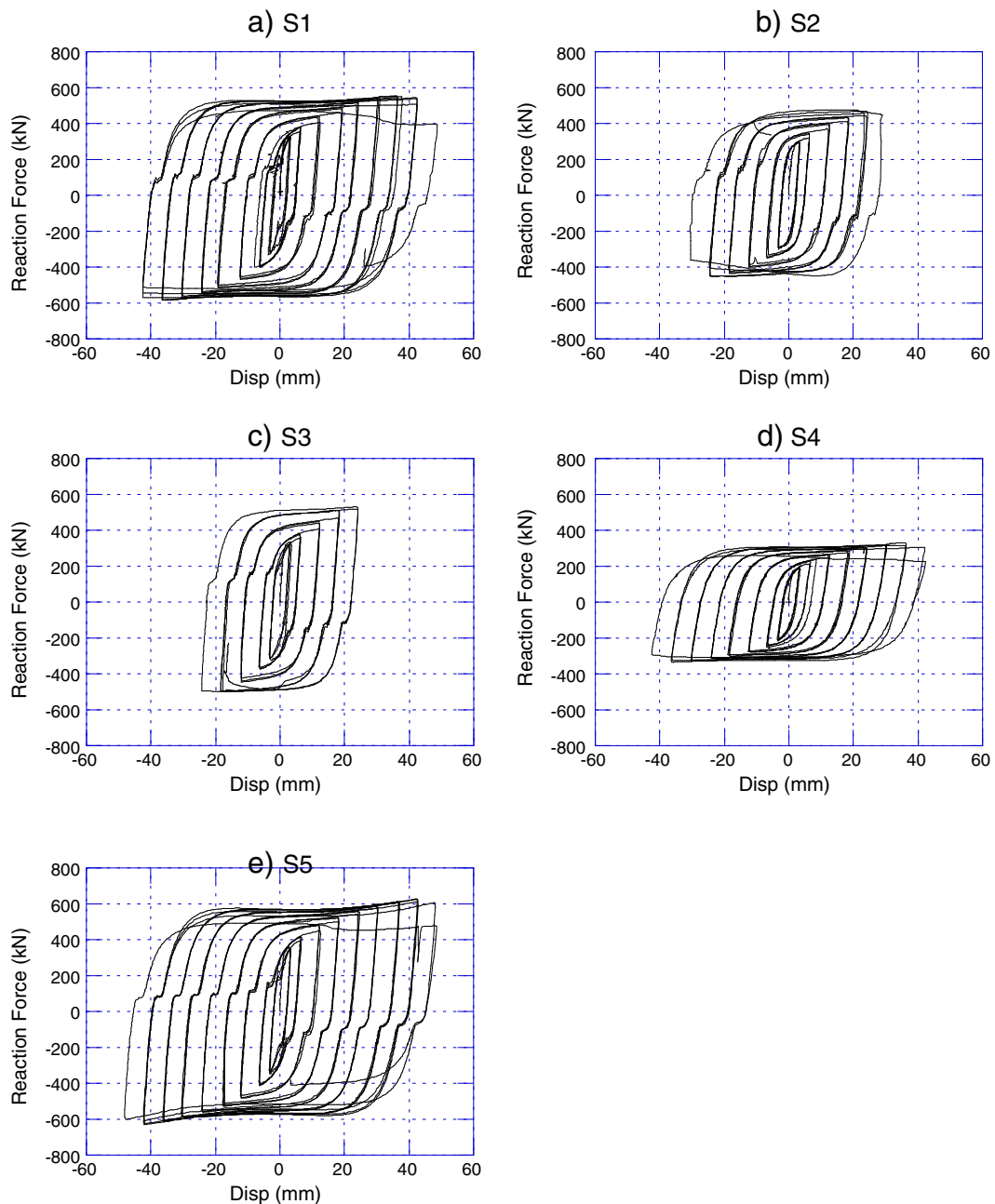


Fig. 7. Hysteresis curve.

Table 2
Results of tests.

No.	Stiffness (kN/mm)	Yield strength (kN)	Ultimate strength (kN)
S1	233	270	568
S2	223	250	462
S3	236	272	515
S4	134	176	332
S5	244	287	629

the energy dissipation plate. S5 lost its capacity at the third cycle of loading at an amplitude of 48 mm.

In Fig. 7a–e, except Fig. 7d, small sharps in the curves appear when the loading direction changes. This is a typical feature of the reversal of the diagonal tension field in shear panels [22–24]. The webs of S1, S2, S3, and S5 are twice as large as that of S4 and the diagonal tension field is easier to form. Hence, these small sharps did not appear in the hysteresis curves of S4.

Table 2 shows the stiffness, yield strength, and ultimate strength of the five specimens. To exclude the influences of buckling, the data measured for the second cycle of loading at an amplitude of 6 mm are selected for the calculation of the stiffness of the specimens.

We noted that except for S4, the stiffness and yield strength of the four specimens were very close. The stiffness and yield strengths were mainly controlled by the width of the web, while the thickness of the side flanges had little effect.

However, the ultimate strengths of the five specimens all differed. The side flanges of S2 and top flange of S3 buckled severely. The ultimate strengths of S2 and S3 were significantly smaller than that of S1. S5 had two horizontal stiffeners and its ultimate strength was greater than that of S1. Thus, we conclude that the horizontal stiffeners improving the ultimate strength and deformation capacity.

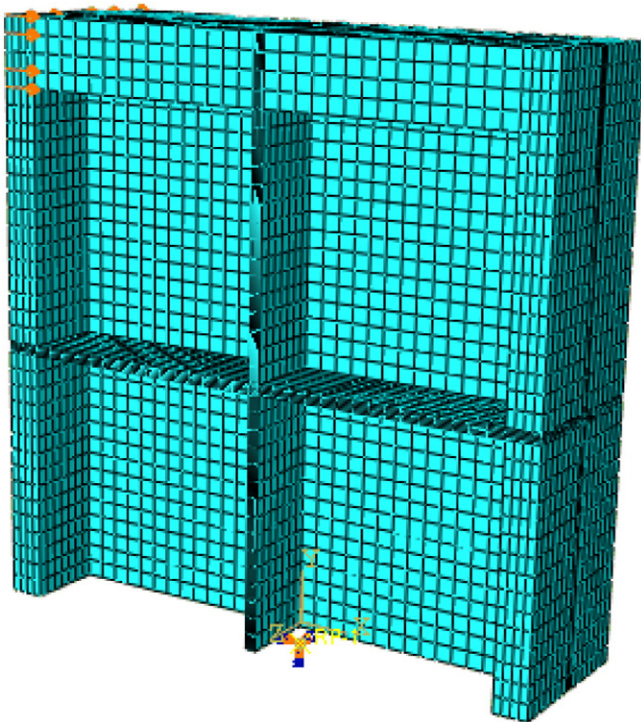


Fig. 8. Finite element model of energy dissipation plate.

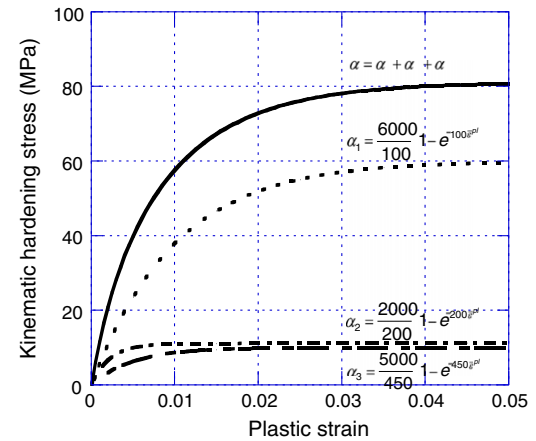


Fig. 9. Kinematic hardening in the numerical material law.

5. Finite element analyses

5.1. Verification of the FE model

Because the number of specimens was rather limited, finite element (FE) analyses were carried out to supplement the physical tests. The general FE software ABAQUS was adopted for the simulation of the restrainer. The FE model is shown in Fig. 8. The energy dissipation plate was simulated with an 8-node reducing integration with an hourglass controlled linear brick element (C3D8R). The FE model had 24,329 nodes and 18,150 elements.

In this study, the specimens were all made of LY225 steel, which has a relatively low yield stress and good low-cycle fatigue performance [25, 26]. As in a previous study, the mechanical performance of steel under cyclic loading was different from that under monotonic loading [27, 28]. The performance of steel under cyclic loading depends on the type of steel, maximum loading amplitude, and loading reversals. Isotropic hardening of low yield point steel is more significant than that of ordinary steel. ABAQUS provided a constitutive model for metal under cyclic loading, see details below.

$$\alpha = \sum_{k=1}^n \frac{C_k}{\gamma_k} \left(1 - e^{-\gamma_k \bar{\epsilon}^{pl}} \right). \quad (5)$$

Eq. (5) is the back stress and hardening stress formula in the material model. α represents the back stress, which indicates the movement of the yield surface. $\bar{\epsilon}^{pl}$ is the equivalent plastic strain (PEEQ). C_k and γ_k are the parameters. This model is the sum of an exponential strain-stress curve. $\sum C_k/\gamma_k$ was the ultimate kinematic hardening stress of the model. In the model, three curves were used to describe the behaviors of steel as shown in Fig. 9. The isotropic hardening was defined by tabular data (Table 3). According to the coupon test the yield stress was 205 MPa. The Young's modulus and Poisson ratio were 206 GPa and 0.3, respectively.

Using the parameters given in Table 3, FE analyses were carried out, and the results obtained were compared with those obtained from the physical tests. The comparisons are as shown in Fig. 10. Fig. 10a, d, g, j, and m compares the hysteresis curves obtained from the physical tests with those of the FE analyses for S1, S2, S3, S4, and S5, respectively. The deformation modes were also compared for the five specimens. The FE analysis results agreed very well with those obtained from the

Table 3
Data for isotropic hardening in numerical material law.

PEEQ	0	0.54	1.113	1.86	2.8	4.3
Hardening stress (MPa)	0	15	20	25	30	35

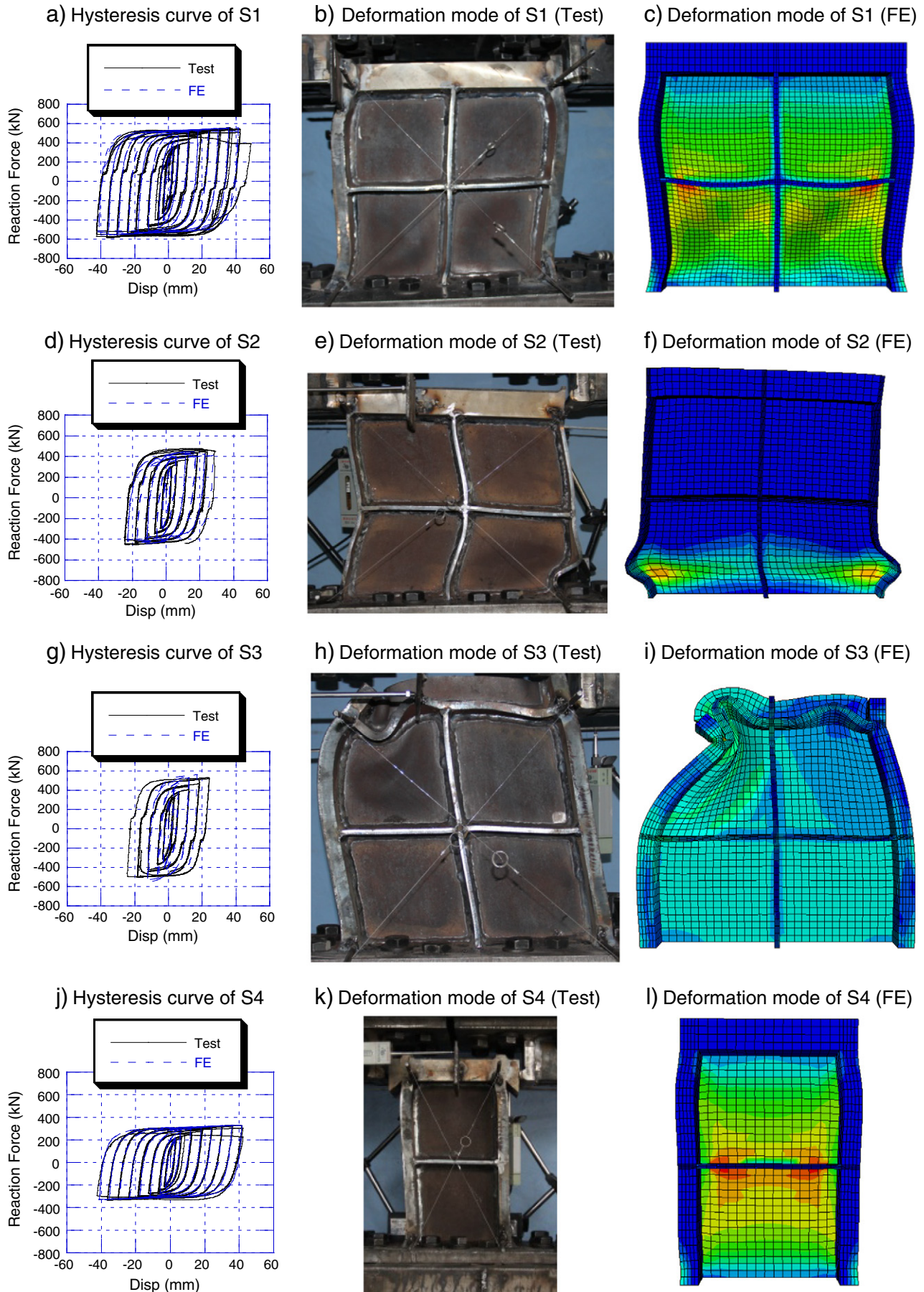


Fig. 10. Comparisons of results obtained from FE analyses and physical tests.

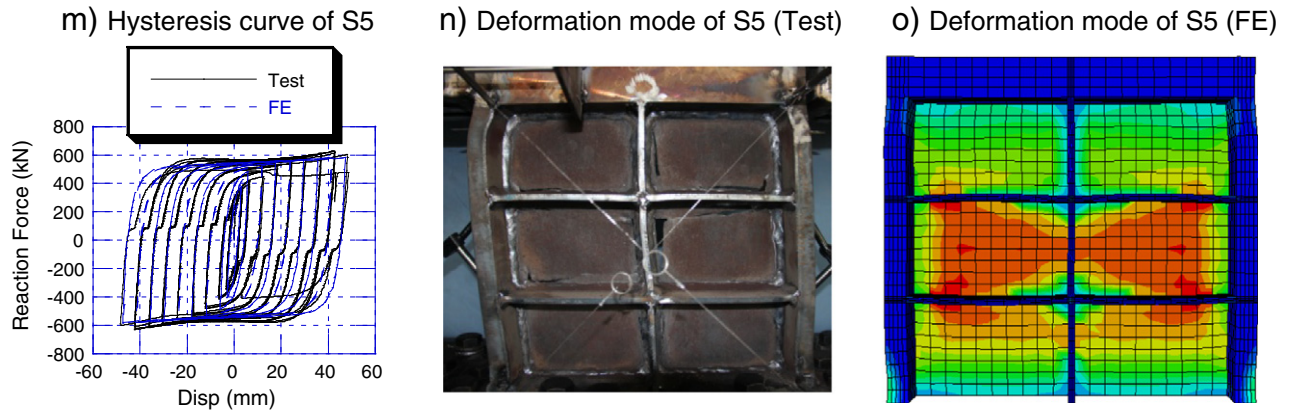


Fig. 10 (continued).

physical tests, demonstrating the effectiveness of the FE models. It should be noted that the numerical model was designed to obtain the quantitative macroscopic mechanical properties of the restrainer, thus the accuracy of the numerical model is insufficient to clearly present the features of the reversal of the diagonal tension field. Hence, the small sharps in the hysteresis curves do not appear in the numerical model.

Note that for Fig. 10m, the experimental strength decreases in the last cycle, which is significantly different from the results of the FE model. The main reason is that there is no low-cycle fatigue damage that was not included in the material properties simulated in the FE model. In the FE analysis the restoring force would not decrease when the low cycle fatigue damage occurred, as in the physical test. Therefore, the PEEQ can be taken as a quantitative characterization of the amount of low-cycle fatigue of the restrainer.

The low-cycle fatigue performance had a positive relationship with PEEQ [29,30]. Fig. 10c, f, i, l, and o shows the PEEQ distribution of the energy dissipation plates for S1, S2, S3, S4, and S5, respectively. The locations of the maximum PEEQ obtained from the FE analyses coincided with those of the low cycle fatigue cracks initiated during the physical tests for S1, S4, and S5. The FE analyses also show that the maximum PEEQs of S1, S4, and S5 are 6.66, 6.66, and 6.56, respectively, when the analyses attempted to simulate the physical loading process. The maximum PEEQs of S1, S4, and S5 are very close, showing that the low cycle fatigue damage will appear when the maximum PEEQ reaches 6.66 for this type of LY225 steel.

5.2. Parametric study

Because the number of specimens in the physical tests was rather limited, FE analyses were conducted to quantitatively analyze the effect of the width of the web and thickness of the side flanges. According to

the physical test results, S5 had the best deformation capacity and greatest strength, showing that having two horizontal stiffeners was helpful in preventing the local buckling of the energy dissipation plate. Therefore, in the supplementary analyses the FE models all had two horizontal stiffeners. Because the results of the buckling analysis are sensitive to the type and size of the element, loading pattern, and numerical parameters, the accuracy of the buckling analysis is difficult to verify. In a conservative approach the thickness of the top flange remained 40 mm, which was shown to be reliable in the physical tests. Based on practical engineering considerations, the space for the restrainer is about 400 mm. therefore, the web cannot be too high. On the other hand, reducing the height of the web would lead to a weak deformation capacity of the restrainer. Therefore, in the parametric analysis the web height of the restrainer remained 300 mm. The FE models also adopted the same height for the web and the same thickness for the top flange in the supplementary specimen. The parameters focused on were the thickness of the side flange and width of the web (Table 4). The loading scheme was the same as in the physical test, with a maximum loading displacement of 48 mm.

The hysteresis curves and deformation modes of the supplementary FE models are shown in Fig. 11. In Fig. 11a, the hysteresis curve of SF8 degrades significantly. The strength of SF8 decreased to 83% of the maximum strength when the loading displacement reached 42 mm, and the side flange buckled significantly, as shown in Fig. 11b. The analysis shows that the maximum PEEQ of SF8 was 21.98, and the plastic strain was concentrated on the side flanges. This was because the thickness of the side flanges was inadequate.

The other eight FE models, i.e., SF12, SF14, SF16, SF18, W200, W225, W250, and W275, had satisfactory hysteresis curves. These eight FE models together with S5 were used for the parametric analysis and to obtain a quantitative formula for estimating the ultimate strength of the restrainer. Table 5 shows the ultimate strength, the loading step when the maximum PEEQ reached 6.6, and the maximum PEEQ after three cycles of loading at an amplitude of 48 mm for the nine models. Note that these nine specimens all have adequate strength and deformation capacity.

The results indicate that the ultimate strength of the restrainer is mainly controlled by the width of web. The thickness of the side flanges b also has some effect on the ultimate strength. Eq. (6) provides a simple means to estimate the ultimate strength of the restrainer. f_u is the ultimate stress of the steel and t_w is the thickness of the web. Note that Eq. (6) assumes that the web sustains pure shear deformation.

$$Q = \frac{f_u t_w (w + 2b)}{\sqrt{3}} \quad (6)$$

Table 4

Parameters of supplementary FE models.

No.	b (mm)	w (mm)
SF8	8	300
SF12	12	300
SF14	14	300
SF16	16	300
SF18	18	300
W200	20	200
W225	20	225
W250	20	250
W275	20	275

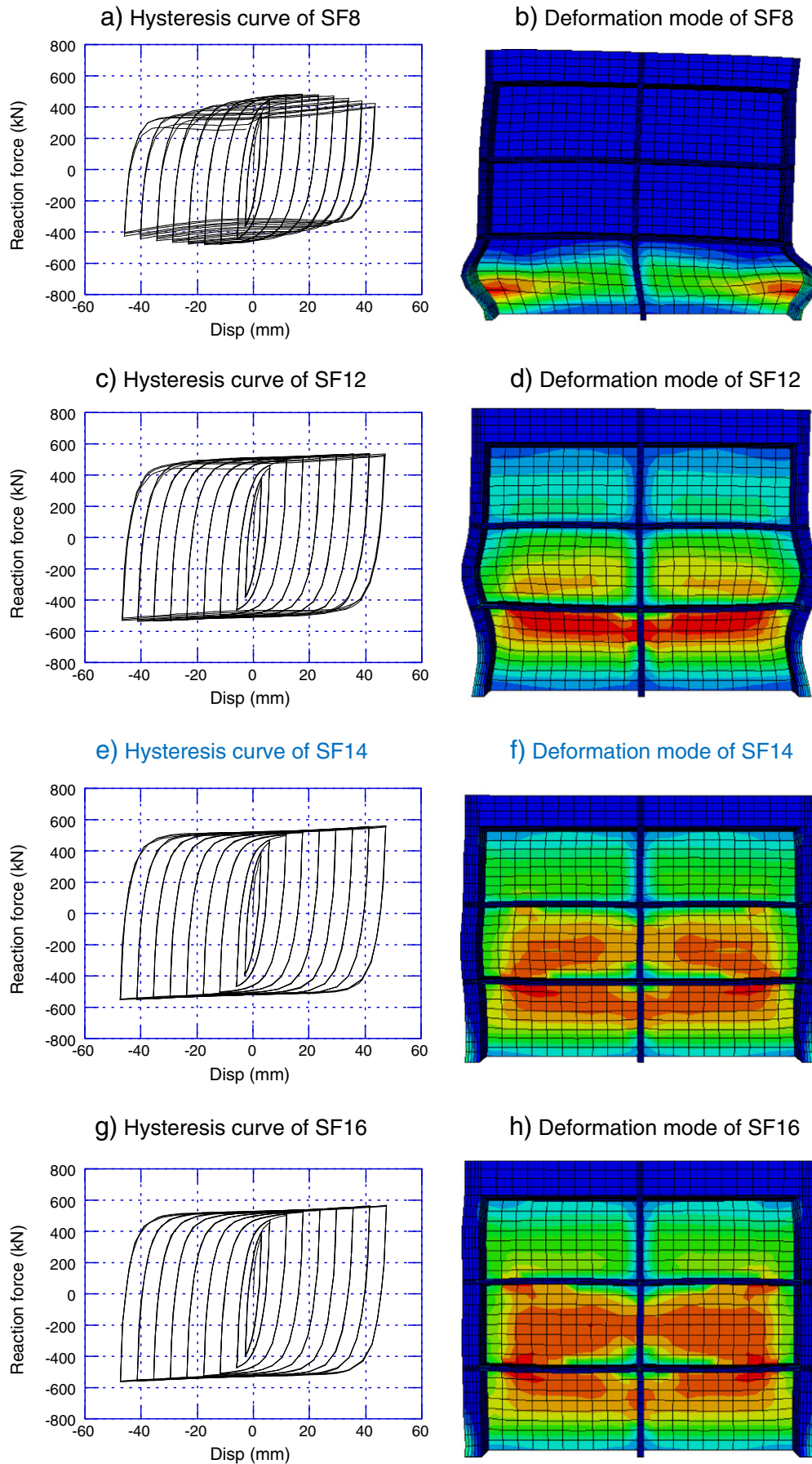


Fig. 11. Hysteresis curve and deformation mode of supplementary models.

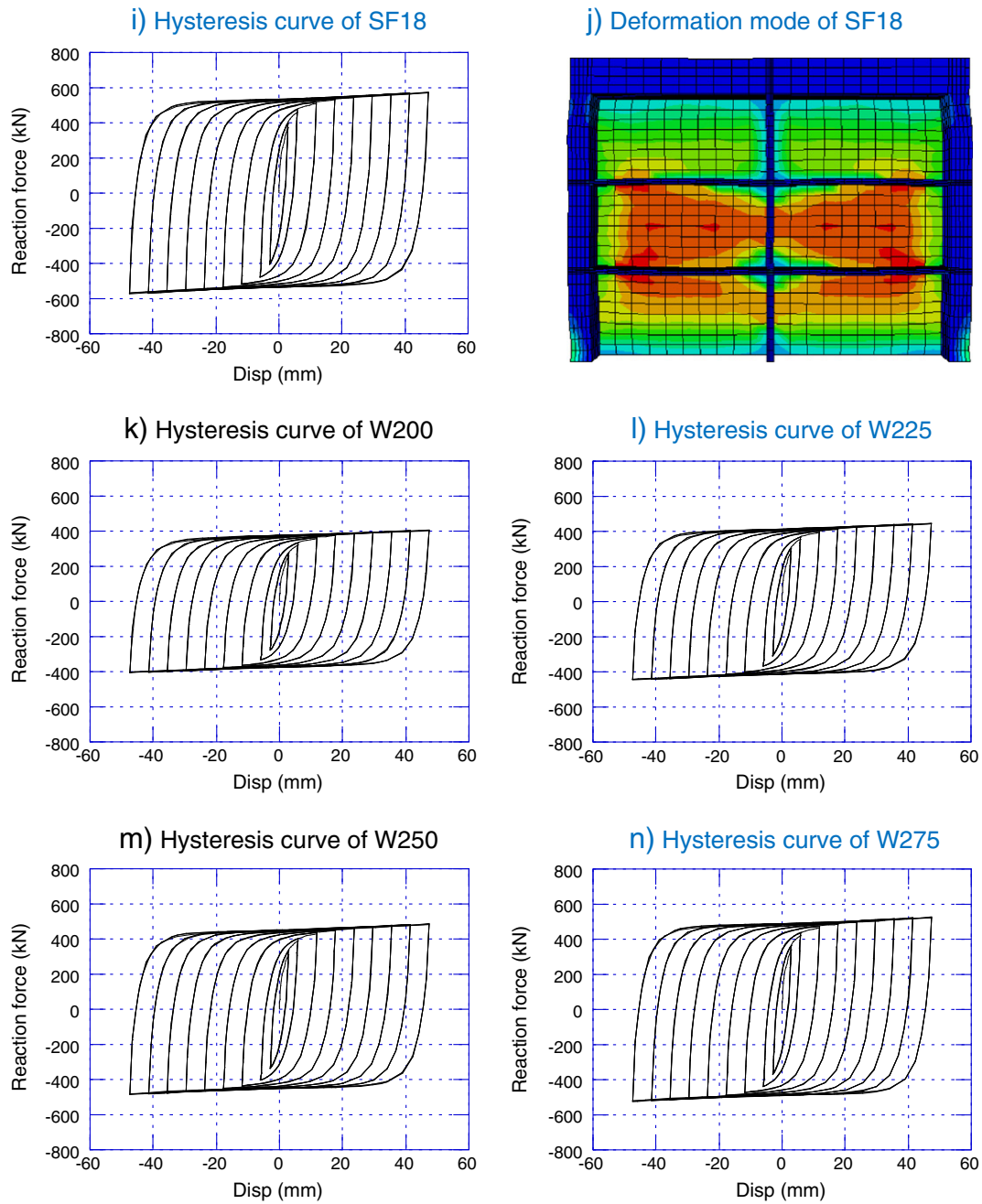


Fig. 11 (continued).

Table 5 compares the results obtained using Eq. (6) with those obtained from the FE analyses. We found that the relative error was large. This was mainly because the side flanges could buckle

and the energy dissipation plate may not sustain pure shear deformation, consequently Eq. (6) overestimated the ultimate strength of the restrainer.

Table 5
Results for nine models.

	Ultimate strength (kN)	Loading step for PEEQ = 6.6	Ultimate PEEQ	Eq. (6) (kN)	Relative error	Eq. (7) (kN)	Relative error
S5	583.68	1st cycle of 48 mm	7.71	690.32	18.27%	577.23	−1.10%
SF12	538.93	1st cycle of 48 mm	9.06	690.32	28.09%	545.00	1.13%
SF14	559.22	1st cycle of 48 mm	7.91	690.32	23.44%	554.53	−0.84%
SF16	565.97	1st cycle of 48 mm	7.64	690.32	21.97%	562.92	−0.54%
SF18	575.10	1st cycle of 48 mm	7.60	690.32	20.03%	570.43	−0.81%
W200	407.69	1st cycle of 48 mm	8.08	487.28	19.52%	407.46	−0.06%
W225	447.40	1st cycle of 48 mm	7.97	538.04	20.26%	449.90	0.56%
W250	487.04	1st cycle of 48 mm	7.85	588.80	20.89%	492.35	1.09%
W275	526.54	1st cycle of 48 mm	7.74	639.56	21.46%	534.79	1.57%

Table 6
Comparisons of Eq. (7).

NO.	<i>b</i> (mm)	<i>w</i> (mm)	Ultimate strength (kN)	Eq. (7) (kN)	Relative error
AD1	15	240	438.66	443.79	1.17%
AD2	17	260	487.66	490.10	0.50%

The side flanges have an influence on the deformation mode of the restrainer. Therefore, Eq. (7), which considers the slenderness of the side flanges, was proposed. In the equation, $(b/h)^\beta$ considers the buckling of the side flanges, and α is a coefficient.

$$Q = \alpha \left(\frac{b}{h} \right)^\beta \frac{f_u t_w w}{\sqrt{3}}. \quad (7)$$

Based on the data from Table 5, a parameter fitting analysis was carried out. It was established that $\alpha = 1.134$ and $\beta = 0.1125$. R-square, which is the square of the correlation between the actual and predicted response values, was equal to 0.992. A value close to 1.0 indicates that a large proportion of variance can be accounted for by the model [31]. The accuracy of Eq. (7) was satisfactory, with relative errors of no more than 1.6%. To investigate the effectiveness of Eq. (7), two additional models, AD1 and AD2, were created in ABAQUS. The parameters and the analysis results of the two models are presented in Table 6. The estimations following Eq. (7) are presented in Table 6. The maximum relative error is 1.17%, demonstrating the effectiveness of Eq. (7).

Finally, the design procedure for the energy dissipation plate can be derived. First, choose the thickness of the web, side flanges, and top flange. We conservatively suggest that the thickness of the top flange and side flanges should be larger than 40 and 16 mm, respectively. Second, determine the height of the web based on the installation space available and practical engineering factors. Third, calculate the width of the web according to Eq. (7). We also recommend that the spacing of the stiffener does not exceed the value of S5.

6. Conclusions

A novel energy dissipation restrainer is proposed in this study. Physical tests were conducted to investigate its performance. The results show that the novel restrainer with a reasonable structure had good strength and deformation capacity. As a supplement, FE analyses were carried out. Formulas for the ultimate strength of the restrainer were proposed and improved based on the tests and FE analysis results. The major conclusions are as follows:

- (1) A restrainer with a reasonable structure has a stable and saturated hysteresis curve and appears similar to a shear panel damper. However, the vertical free mechanism and large concentrated force from the horizontal locking device require the side flanges and top flanges of the energy dissipation plate to have a sufficient thickness to avoid instability failure during earthquakes.
- (2) The vertical free mechanism may lead to instability failure at the side flanges. The horizontal stiffener of the energy dissipation plate restricts the buckling of the web and side flanges at the same time. Therefore, the energy dissipation plate needs more stiffeners than the common steel shear panel damper, especially in the horizontal direction.
- (3) With the help of finite element analysis the quantitative formula for the ultimate restoring force was obtained and the design procedure of the restrainer was derived. Some important suggestions about the structure of the stiffener and flanges are proposed.

Acknowledgments

We gratefully acknowledge the financial support of the National Natural Science Foundation of China under grant Nos. 50808107, 51178250, and 51261120377, and of the Tsinghua University of China under Grant No. 2010Z01001.

References

- [1] Fennes GL, DesRoches R. Response of the northwest connector in the Landers and Big Bear earthquakes[R]. Earthquake Engineering Research Center, University of California; 1994.
- [2] Wang Dongsheng, Guo Xun, Sun Zhiguo, Meng Qingli, Yu Dehai, Li Xiaoli. Damage to Highway Bridge during Wenchuan Earthquake [J]. J Earthq Eng Eng Vib 2009;29(3):84–94 (In Chinese).
- [3] Kawashima K, Unjoh S, Hoshikuma J, Kosa K. Damage of transportation facility due to 2010 Chile earthquake (April 5, 2010). Bridge Team Dispatched by Japan Society of Civil Engineers; 2010.
- [4] Priestley MJN. Seismic design and retrofit of bridges [M]. Wiley.com; 1996.
- [5] Jónsson MH, Bessason B, Haflidason E. Earthquake response of a base-isolated bridge subjected to strong near-fault ground motion [J]. Soil Dyn Earthq Eng 2010;30(6):447–55.
- [6] Schanack F, Valdebenito G, Alvia J. Seismic damage to bridges during the 27 February 2010 magnitude 8.8 Chile earthquake [J]. Earthquake Spectra 2012;28(1):301–15.
- [7] Chaudhary MTA, Abé M, Fujino Y. Investigation of atypical seismic response of a base-isolated bridge[J]. Eng Struct 2002;24(7):945–53.
- [8] DesRoches R, Muthukumar S. Effect of pounding and restrainers on seismic response of multiple-frame bridges [J]. J Struct Eng 2002;128(7):860–9.
- [9] Ghosh G, Singh Y, Thakkar SK. Seismic response of a continuous bridge with bearing protection devices[J]. Eng Struct 2011;33(4):1149–56.
- [10] DesRoches R, Delemont M. Seismic retrofit of simply supported bridges using shape memory alloys [J]. Eng Struct 2002;24(3):325–32.
- [11] Wilde K, Gardoni P, Fujino Y. Base isolation system with shape memory alloy device for elevated highway bridges [J]. Eng Struct 2000;22(3):222–9.
- [12] Sharabash AM, Andrawes BO. Application of shape memory alloy dampers in the seismic control of cable-stayed bridges [J]. Eng Struct 2009;31(2):607–16.
- [13] Billah AHM, Alam MS, Bhuiyan AR. Seismic performance of a multi-span bridge fitted with superelastic SMA-based isolator [C]. Intl. Proc. IABSE-JSCE Joint Conference on Advances in Bridge Engineering-II; 2010. p. 8–10.
- [14] Morgan NB, Friend CM. A review of shape memory stability in NiTi alloys[J]. J Phys IV 2001;11(PR8) (Pr8-325-Pr8-332).
- [15] Norfleet DM, Sarosi PM, Mancharaju S, et al. Transformation-induced plasticity during pseudoelastic deformation in Ni–Ti microcrystals [J]. Acta Mater 2009;57(12):3549–61.
- [16] HUBE MA, RUBILAR F. Capacity evaluation of steel restrainers of reinforced concrete Chilean bridges[C]. The International Symposium for the 25th Anniversary of the CISMID; 2012. p. 17–8.
- [17] Mitoulis S, Tegos J. Reduction of inertial seismic forces in bridges by using the abutment backwall as a “yielding” stopper. Earthquake Resistance Structures, Skiathos, Greece: Proceedings; 2005 507–20.
- [18] Nakashima M, Iwai S, Iwata M, Takeuchi T, Konomi S, Akazawa T, et al. Energy dissipation behaviour of shear panels made of low yield steel [J]. Earthq Eng Struct Dyn 1994;23(12):1299–313.
- [19] Tanaka K, Sasaki Y. Hysteretic performance of shear panel dampers of ultra-low-yield-strength steel for seismic response control of buildings[C]. 12th World Conference on Earthquake Engineering. New Zealand: WCEE; 2000.
- [20] Zhang Chaofeng, Zhang Zhisheng, Zhang Qiuju. Static and dynamic cyclic performance of a low-yield-strength steel shear panel damper [J]. J Constr Steel Res 2012;79:159–203.
- [21] Ji X, Jiang F, Qian J. Seismic behavior of steel tube–double steel plate–concrete composite walls: experimental tests [J]. J Constr Steel Res 2013;86:17–30.
- [22] Jianguo NIE, Jiansheng FAN, Yuan HUANG, Wei ZHOU, Dasui WANG, Daoyuan LU. Experimental research on steel plate shear wall. J Build Struct 2010;31(9):1–8 (In Chinese).
- [23] Kaminski BE, Ashton JE. Diagonal tension behavior of boron-epoxy shear panels [J]. J Compos Mater 1971;5(4):553–8.
- [24] Chan RWK, Albermani F, Kitipornchai S. Experimental study of perforated yielding shear panel device for passive energy dissipation [J]. J Constr Steel Res 2013;91:14–25.

- [25] Ge H, Chen X, Matsui N. Seismic demand on shear panel dampers installed in steel-framed bridge pier structures [J]. *J Earthq Eng* 2011;15(3):339–61.
- [26] Ge HB, Kaneko K, Usami T. Capacity of stiffened steel shear panels as a structural control damper[C]. *The 14th World Conference on Earthquake Engineering (14WCEE)*; 2008.
- [27] Shi Y, Wang M, Wang Y. Experimental and constitutive model study of structural steel under cyclic loading [J]. *J Constr Steel Res* 2011;67(8):1185–97.
- [28] Dusicka P, Itani AM, Buckle IG. Cyclic response of plate steels under large inelastic strains [J]. *J Constr Steel Res* 2007;63(2):156–64.
- [29] Iyama J, Ricles JM. Prediction of fatigue life of welded beam-to-column connections under earthquake loading [J]. *J Struct Eng* 2009;135(12):1472–80.
- [30] Deng K, Pan P, Wang C. Development of crawler steel damper for bridges [J]. *J Constr Steel Res* 2013;85:140–50.
- [31] Curve fitting Toolbox User's Guide [M]. MathworksInc; 2010.